

# Topological cascade of quantum Borromean rings

Cite as: Phys. Fluids **37**, 024126 (2025); doi: 10.1063/5.0252708

Submitted: 11 December 2024 · Accepted: 21 January 2025 ·

Published Online: 20 February 2025



View Online



Export Citation



CrossMark

Hao Guan (关昊),<sup>1</sup> Simone Zuccher,<sup>2</sup> and Xin Liu (刘鑫)<sup>1,a)</sup>

## AFFILIATIONS

<sup>1</sup>Institute of Theoretical Physics, Beijing University of Technology, Beijing 100124, People's Republic of China

<sup>2</sup>Department of Computer Science, University of Verona, Ca' Vignal 2, Strada Le Grazie 15, 37134 Verona, Italy

<sup>a)</sup>Author to whom correspondence should be addressed: [xin.liu@bjut.edu.cn](mailto:xin.liu@bjut.edu.cn)

## ABSTRACT

The evolution and the topological cascade of quantum vortices forming Borromean rings are studied for the first time. The initial configuration of the system is given by three elliptical planar loops linked together, and the evolution is governed by the numerical implementation of the Gross–Pitaevskii equation. It is found that the topological cascade is not unique, but it depends crucially on the initial geometric configuration. Quantum vortices undergo a series of spontaneous reconnections, resulting in various degenerative pathways characterized by different topology and structural complexity triggered by the different inclination of one of the initial ellipses. Typical decaying routes are given by the successive creation of a Whitehead link, a connected sum of two Hopf links, a trefoil knot, a Hopf link, and the final formation of unknotted, unlinked loops. By structural complexity analysis, we show that the generic trend of the vortex decay goes through a series of topological simplifications, resulting in the formation of small-scale planar loops (rings). During the later stage of evolution, the inverse cascade and topological cycles involving the interaction of unknotted loops become more common, remaining subdominant to the overall topological simplification process. These results pave the way to investigate the fundamental relations between structural complexity and energy contents.

Published under an exclusive license by AIP Publishing. <https://doi.org/10.1063/5.0252708>

## I. INTRODUCTION

In this paper, we address the question of the topological cascade of three quantum vortex loops linked together to form a system of Borromean rings evolving under the Gross–Pitaevskii equation (GPE). The initial configuration of these quantum vortices provides the best compromise between a simple superfluid vortex tangle and a realizable topologically complex system of defects (more complicated than the cases of interacting line strands, Hopf link<sup>1–3</sup>); in this sense, this work aims to fill the gap between the study of simple interactions between quantum vortices and quantum turbulence. Indeed, with the proposed test, we expect to understand the geometric and topological features of a decaying process experienced by quantum vortices through a series of interaction/reconnection events, till the final creation of unknotted, unlinked loops. The experiment is carried out by direct numerical implementation of the Gross–Pitaevskii equation (GPE). Our study on the different cascade routes clarifies the importance and probability that a particular decaying path appears to have with respect to others. The emphasis of the present work is on the topological aspects of the cascade process, whereas the associated dynamics and energetics will be discussed in another paper.

Work on the dynamics of quantum vortices governed by the GPE has grown extensively in recent years,<sup>4</sup> from defect

interactions<sup>5,6</sup> and reconnections<sup>1,7–11</sup> to creation and evolution of complex tangles in quantum turbulence.<sup>12–16</sup> Researchers have paid attention also to geometric and topological characterization of interacting structures as well, with emphasis on the relation between morphological aspects and dynamical considerations.<sup>2,17–20</sup> The discovery of a variety of knots and links formed during quantum turbulence production<sup>21,22</sup> has strengthened the interest in the actual mechanism of creation and re-organization of topologically complex structures,<sup>3,23,24</sup> especially in relation to the open question of defects' energy transfer and localization during an evolution procedure. The present analysis of the decay of quantum Borromean rings is, indeed, inspired by the remarkable similarities of the topological cascade of knotted vortices in water,<sup>25</sup> magnetic tubes,<sup>26</sup> classical flow,<sup>27</sup> and the DNA catenanes in biology,<sup>28</sup> and by the theoretical prediction of optimal pathways based on knot polynomial invariants in an algebraic space.<sup>29,30</sup>

This paper is arranged as follows. In Sec. II, we present the numerical implementation of the governing equation and the initial conditions. In Sec. III, the leading decaying paths are discussed, and an evolution map is presented. In Sec. IV, key aspects associated with different topological patterns (such as statistics, bifurcation, and trend features) are pointed out. Conclusion is drawn in Sec. V.

## II. GOVERNING EQUATION, INITIAL CONDITIONS, AND NUMERICAL SETUP

We study the evolution of three closed vortex loops initially forming Borromean rings [see Figs. 1(a) and 1(b)]. Their dynamics is governed by the Gross–Pitaevskii equation (GPE),<sup>31,32</sup> which, in the non-dimensional form, reads

$$\frac{\partial \Psi}{\partial t} = \frac{i}{2} \nabla^2 \Psi + \frac{i}{2} (1 - |\Psi|^2) \Psi, \quad (1)$$

where  $\Psi = \Psi(\mathbf{x}, t)$  is the condensed matter wavefunction depending on the space  $\mathbf{x}$  and the time  $t$ ,  $i$  denotes the imaginary unit, and  $\nabla^2$  is the Laplace operator. The aforementioned equation conserves total mass and total energy, together with linear and angular momentum.

The initial condition for the quantum vortices is given by three inter-linked closed curves  $C_i$  ( $i = 1, 2, 3$ ) of the wavefunction forming planar ellipses. In the ideal symmetric case, the latter belong to mutually orthogonal planes, as shown in Fig. 1(c). The vortex circulation is taken to be constant and equal to  $2\pi$  for all the defects (no multiply charged vortices are considered), the fluid density  $\rho \rightarrow 1$  as  $\mathbf{x} \rightarrow \infty$ . According to the fourth-order Padé approximation,<sup>33–35</sup> the fluid density  $\rho = |\Psi|^2$  is given by

$$\rho(r) = \frac{a_1 r^2 + a_2 r^4 + a_3 r^6 + a_4 r^8}{1 + b_1 r^2 + b_2 r^4 + b_3 r^6 + a_4 r^8}, \quad (2)$$

where  $r$  denotes the radial distance from a point on the vortex line, and the coefficients  $a_i, b_i$  can be found in Ref. 34 together with the details of the whole derivation for the Padé approximation. For a given point  $P$  in space, not on the vortex line, the wavefunction  $\Psi(\mathbf{x}_P, t)$  is computed in two steps: first, we determine the nearest point  $O \in C_i$  to  $P$ , define  $r = |OP|$ , and use Eq. (2) to compute  $\sqrt{\rho(r)} = |\Psi|$ ; second, we compute the angle  $\Theta$  between the unit normal at  $O$  and  $OP$ ,

i.e.,  $\Theta = \arg \Psi$ . For the three Borromean rings, the resulting wavefunction  $\Psi_P$  at  $P$  is instantaneously given by the three contributions of each individual wavefunction, i.e.,

$$\Psi_P = \Psi_{1P} \Psi_{2P} \Psi_{3P} = \sqrt{\rho_1 \rho_2 \rho_3} e^{i(\Theta_1 + \Theta_2 + \Theta_3)}. \quad (3)$$

### A. Numerical setup

The time evolution of the Borromean rings (hereafter denoted by  $\mathbf{B}$  for short) is carried out by the numerical implementation of Eq. (1), prescribing the initial geometry and topology of the quantum vortices. This is done following the same methodology as in Ref. 1, i.e., by employing the second-order Strang splitting approach, in which the linear part (Laplace operator) is solved by the Fourier spectral method.

As described in Ref. 34, Eq. (1) is split into the so-called kinetic and potential parts,

$$\frac{\partial u}{\partial t} = \frac{i}{2} \nabla^2 u, \quad (4a)$$

$$\frac{\partial v}{\partial t} = \frac{i}{2} (1 - |v|^2) v. \quad (4b)$$

Equation (4a) is solved exactly in time after the physical solution is transformed into the Fourier (spectral) space. On the other hand, Eq. (4b) is solved exactly in the physical space as  $|v|$  is preserved by the equation. By introducing  $e^{\tau A} u_n(\mathbf{x})$  and  $e^{\tau B} v_n(\mathbf{x})$  to denote the two partial numerical solutions, the numerical approximation  $\Psi_{n+1}(\mathbf{x})$  of  $\Psi(\mathbf{x}, t_{n+1})$  at time  $t_{n+1} = (n+1)\tau$  is recovered by the so-called Strang splitting,

$$\Psi_{n+1/2}(\mathbf{x}) = e^{\tau A} e^{iB} \Psi_n(\mathbf{x}), \quad (5a)$$

$$\Psi_{n+1}(\mathbf{x}) = e^{iB} \Psi_{n+1/2}(\mathbf{x}). \quad (5b)$$

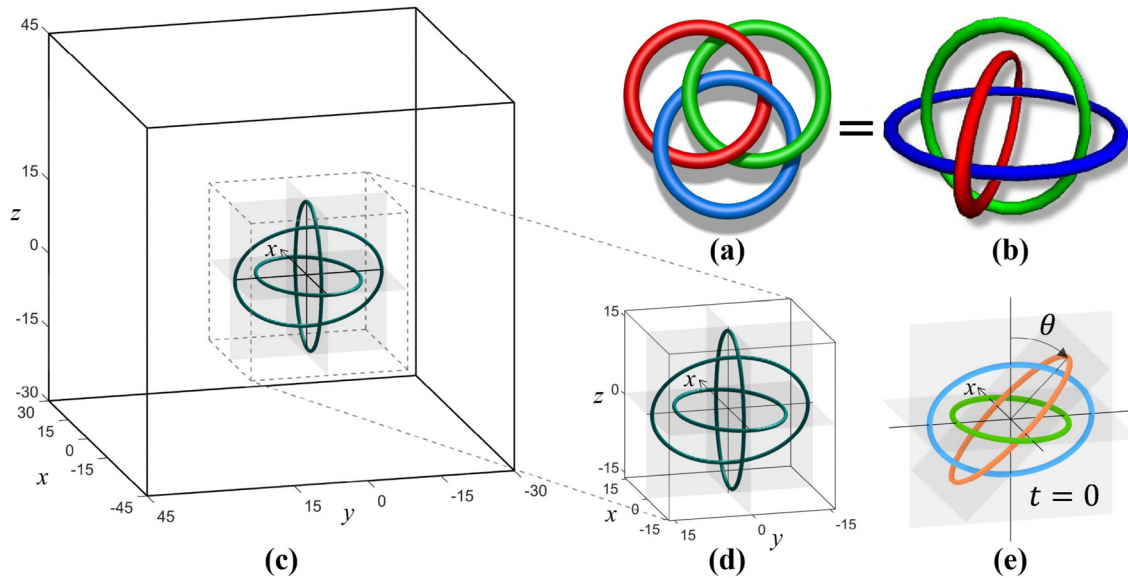


**FIG. 1.** (a) Projection diagram of Borromean rings. (b) 3D representation of the Borromean rings formed by 3 ellipses, which is topologically equivalent to (a). (c) Symmetric configuration: the Borromean rings, visualized by three planar elliptical thin tubes at  $\rho_{iso} = 0.05$ , are centered placed orthogonally to each other in the  $xy$ -,  $yz$ -, and  $xz$ -planes for  $\theta = 0$ . (d) Zoomed-in view of the symmetric initial configuration. (e) Asymmetric configuration: one ellipse is tilted by an angle  $\theta > 0$  from  $xz$ -plane about the  $x$ -axis.

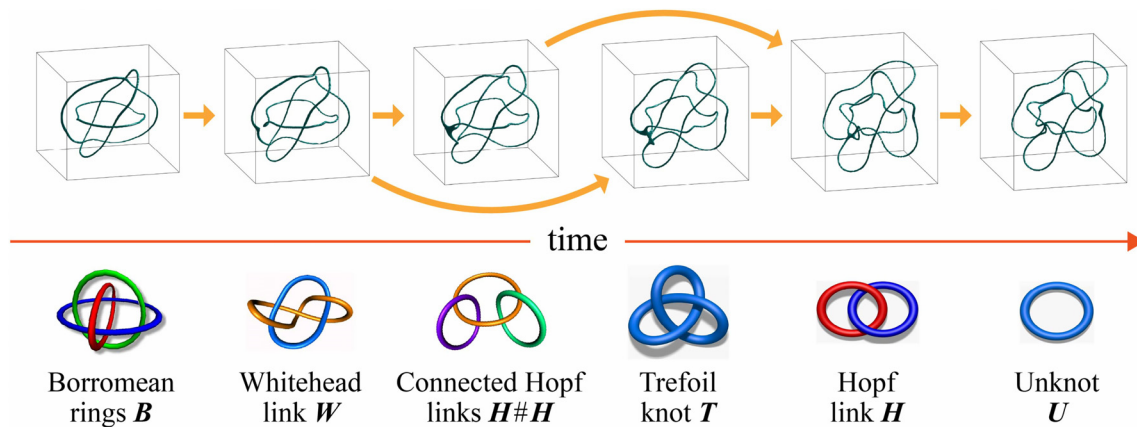


**FIG. 2.** (Top) Zoomed-in snapshots of the main topological states produced during the evolution of quantum vortices under GPE, seen from the same viewing angle. (Bottom) Pictorial representation of the topological states observed at various stages of the decaying path: 6-crossings Borromean rings ( $B$ ), 5-crossings Whitehead link ( $W$ ), 4-crossings connected sum of Hopf links ( $H\#H$ ), 3-crossings trefoil knot ( $T$ ), 2-crossings Hopf link ( $H$ ), and unknotted loop ( $U$ ).

The Strang splitting preserves the discrete finite mass in the computational domain and is second-order accurate in time. Since the time splitting Fourier methods restricted to a bounded physical domain can be applied only in the presence of periodic boundary conditions, initial conditions that are not periodic must be mirrored in the

directions lacking periodicity, with a consequent increase in the degrees of freedom and computational effort.<sup>34</sup>

In our numerical simulations, the quantum vortices of circulation  $2\pi$  are placed in a original domain  $[-45; 30] \times [-30; 45] \times [-30; 45]$  discretized by a  $[225 \times 225 \times 225]$  mesh, so that

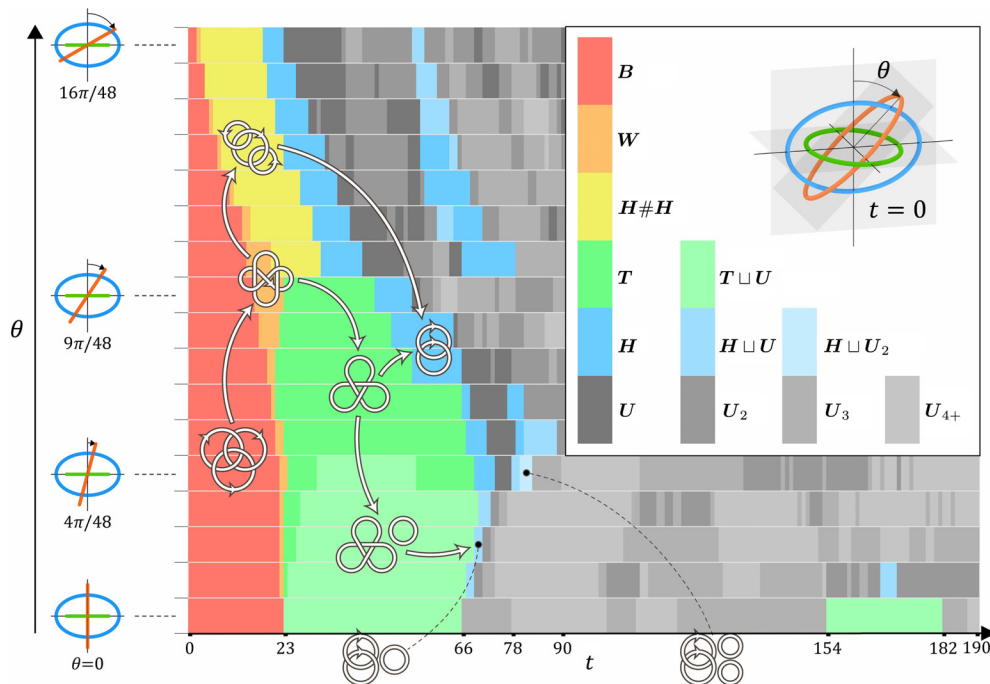


**FIG. 3.** Summary of the topological cascade of the Borromean rings by varying values of  $\theta$ , from 0 to  $16\pi/48$ . By varying  $\theta = k\pi/48$  for  $k \in \{0, 1, \dots, 16\}$ , the initial configuration of the Borromean rings evolves dynamically. Strands interact, reconnect, and form distinct topological types through various pathways. Inset: Colors denote different topological configurations realized during the evolution, as indicated by the different values of  $\theta$ . Vertical axis (left): The values of  $\theta$  as defined in the inset. For simplicity, only 4 of the 17 prescribed values are indicated. Horizontal axis (bottom): Time units are shown for  $t \in [0, 190]$ , with critical time values marking typical topological transitions. Legend: Each colored box represents a specific topology at a given time, characterized by a decreasing topological crossing number  $n$  (from the 6-crossing Borromean rings to the 0-crossing unknotted loop) and an increasing number of unknots. Together, these configurations form a spectrum of topological states.

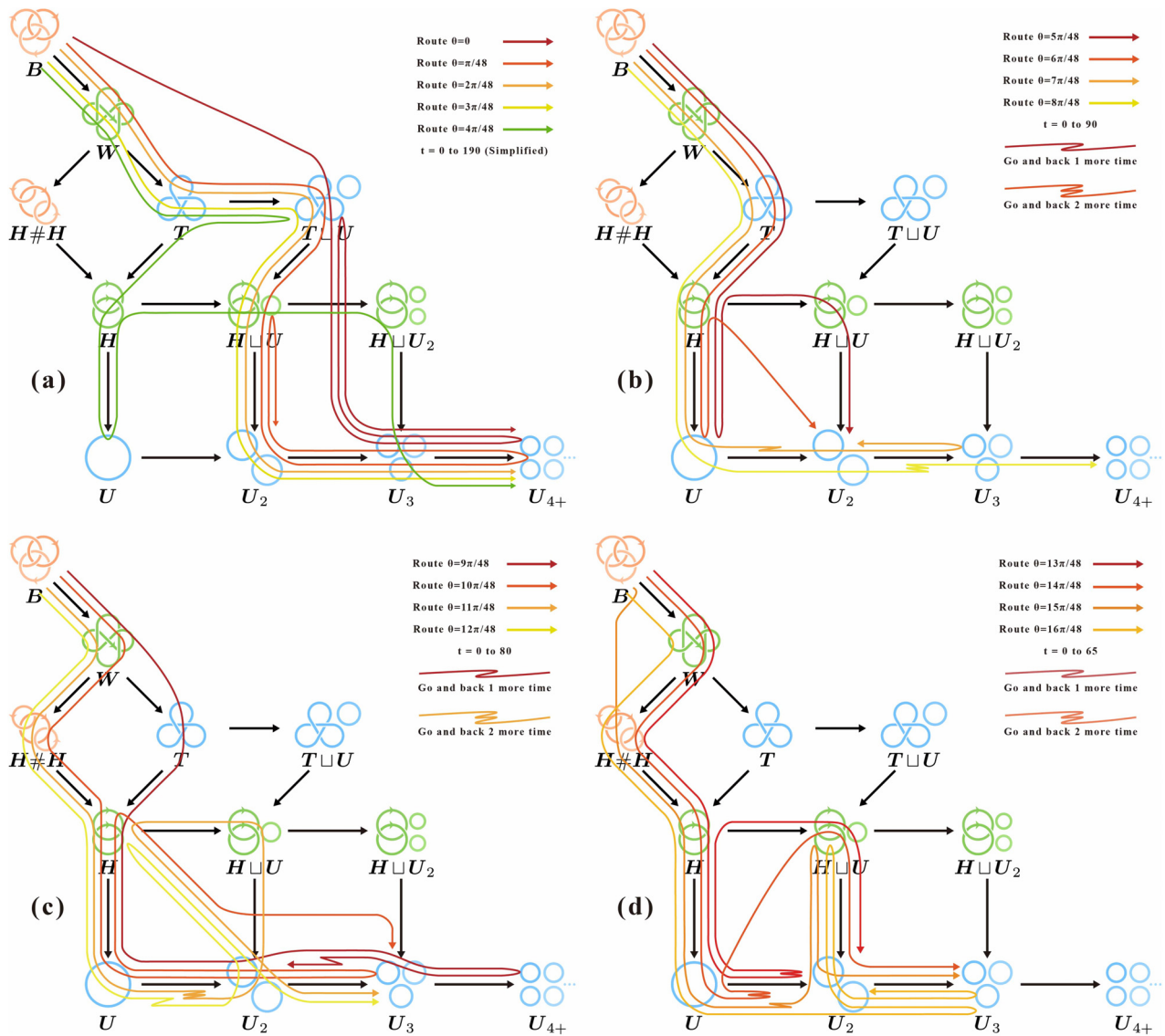


FIG. 4. Evolutionary routes generated by incrementally varying a single geometric parameter  $\theta$  across 17 experiments.

$\Delta x = \Delta y = \Delta z = 1/3$ . The unit length is based on the healing length  $\zeta = 1$ , which corresponds also to the vortex core size. This means that there are three grid points within the vortex core. The initial condition is generated in the original domain, and then it is mirrored in the three spatial dimension to ensure the periodicity required by the Fourier approach. The numerical simulation is then carried out in the mirrored numerical domain made of  $[450 \times 450 \times 450]$  grid points, keeping  $\Delta x = \Delta y = \Delta z = 1/3$ . The time step employed in the Strang splitting method is  $\tau = 1/80$ . Further technical details regarding the numerical method can be found in Ref. 34.

For the ideal symmetric case, the initial configuration is given by three planar ellipses centered in mutually orthogonal planes, as shown in Fig. 1(c). In terms of vortex core size units, the geometry of the three ellipses is given by an aspect ratio of 30/20. The defects are sufficiently

separated from each other and from the boundaries of the computational domain, to avoid undesired effects. As shown in Fig. 1(d), the orientation of the first and second ellipses is  $\mathbf{n}_1 = (0, 0, 1)$  and  $\mathbf{n}_2 = (-1, 0, 0)$ , with the major axes aligned along the  $x$ -axis and  $y$ -axis, respectively. The orientation of the third ellipse is  $\mathbf{n}_3 = (0, \cos \theta, \sin \theta)$  with its major axis belonging to the  $xz$ -plane and tilted by an angle  $\theta$  around the  $x$ -axis from the  $z$ -axis. With the purpose of exploring the effects of geometric perturbations on the decaying routes, we have chosen  $\theta = k\Delta\theta \geq 0$  with  $\Delta\theta = \frac{\pi}{48}$  and  $k = 0, 1, \dots, 16$ , and thus, 17 distinct initial conditions are explored, as shown in Fig. 1(e) and in the illustration on the left vertical axis of Fig. 3. We restrict our investigations to  $\theta \leq 16\pi/48 = 60^\circ$  because above  $\theta = 16\pi/48$ , the distance between vortices may drop below the order of  $o(2\zeta)$ , thus preventing a reliable detection of the

reconnection events. The dynamics of quantum vortices is analyzed in terms of geometry and topology by taking snapshots of the  $\Psi$ -evolution at every time interval  $\Delta t = 1$  (for convenience, noted as “1s”), for the 17 values of  $\theta$  at  $t = 0$ .

Due to the relative vorticity orientation, the defects tend to reconnect and drift collectively in the direction of  $\mathbf{n} = \mathbf{n}_1 + \mathbf{n}_2 + \mathbf{n}_3 = (-1, \cos \theta, 1 + \sin \theta)$  toward the negative  $x$ -axis and along the positive direction of the  $y$ - and  $z$ -axis. During the time evolution, particular attention is paid to highly bent vortices because their high curvature allows them to travel faster, enabling them to quickly reach the boundaries of the computational domain, which may result in unreliable dynamics. As the initial angle of inclination  $\theta$  increases, the special separation between the vortices decreases and leads to earlier reconnections, so that the type of evolution and the variety of decay paths are strongly influenced by the initial values of  $\theta$ .

In this paper, for simplicity, we denote the topologies observed in the simulations without the indices that distinguish the positive and negative types (or, the left-handed and right-handed forms). The actual chiralities of these topologies are detailed in Appendix A, Fig. 8 in particular.

### III. TOPOLOGICAL ANALYSIS OF DECAYING PATHS DURING EVOLUTION

The process of topological evolution occurs in a stepwise manner with several topological states acting as midway stages. Due to variations in initial conditions, vortex reconnections occurring at each stage may differ significantly, leading to a diverse range of decaying paths. This diversity gives rise to observable statistical patterns in the selection of these paths, providing a deeper insight into the underlying mechanisms governing topological transformations.

By analyzing the various decaying paths generated by the 6-crossings Borromean rings  $B$ , we can identify 5 typical topological states produced by the reconnections and visualized by their pictorial representation as shown in Fig. 2. These states are classified according

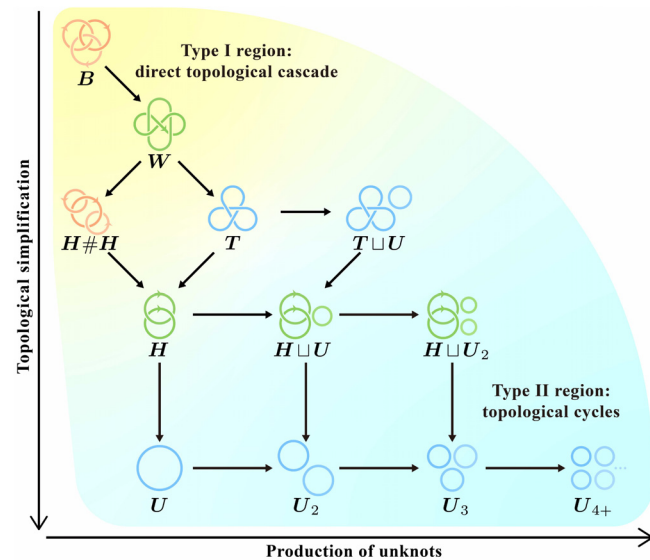


FIG. 5. Type-I and Type-II regions as well as the gradually changing region, identified by the distinguished pattern of topological simplification.

to their topological crossing number and given by the 5-crossing (negative) Whitehead link  $W$ , the 4-crossing connected sum of Hopf links  $H\#H$  (where the  $\#$  symbol denotes the connected sum operation, which combines two knots into a single composite knot), the 3-crossing (left-hand) trefoil knot  $T$ , the 2-crossing (negative) Hopf link  $H$ , and the unknotted loop  $U$ . This sequence represents a family of key topological types produced during the various decaying paths, but the path is neither unique nor reproduced in its entirety by the different pathways.

To describe the specific decaying paths produced by the Borromean rings for each initial configuration prescribed by one of the 17 inclination angles, we must analyze each topological cascade in detail, and, thus, a much richer scenario is obtained, as summarized in Fig. 3. Note that the family of topological states and the transitional paths detected by the present simulations represent only a small subset of all the possible topological states or paths admissible, in principle, by the theoretical analysis based on the minimal diagram projections of knot theory (see Sec. II A and Fig. 8 in Appendix A).

With reference to Fig. 3, since each snapshot corresponds to one time unit, the horizontal extent of a colored region (i.e., a topological type) provides direct information about its persistence before undergoing reconnection, offering a measure of its topological lifetime. Another direct information comes from the total area represented by the colored regions, which is a measure directly related to the topological persistence for various angles. From this, we can evidently conclude that the Whitehead link  $W$  represents a rather short-lived occurrence, whereas the presence of trefoil knots with disjoint, unlinked single loops (denoted by  $T\sqcup U$ ) is a recurrent feature. It should be noted that the aforementioned statistical results are limited to the initial conditions considered in this study. In Ref. 36, for example, the evolution of asymmetrical Borromean rings  $B$  under different initial conditions resulted in a longer-lived Whitehead link  $W$ .

For  $\theta = 0$ , the Borromean rings collapse directly to form first a trefoil knot and an unknot (represented by the disjoint union  $T\sqcup U$ ), then a collection of 3, 4, or more unknots (denoted, respectively, by  $U_3$  and  $U_{4+}$ ), and even a reverse cascade of  $T\sqcup U$ , till the final production of several unknots  $U_{4+}$ . A more elaborate cascade is produced by  $\theta = 9\pi/48$ , where we have

$$B \rightarrow W \rightarrow T \rightarrow H \rightarrow U \rightarrow U_2 \rightarrow U_3 \rightarrow U_{4+} \rightarrow U_{\Delta}, \quad (6)$$

whereby  $U_{\Delta}$  denotes the alternative production of 2 or 3 disjoint unknotted loops. For  $\theta = 16\pi/48$ , we have an initial gradual decrease in crossing numbers from 6 to 4, given by the sequence  $B \rightarrow W \rightarrow H\#H$ , before jumping to the production of Hopf links and unknots. As discussed in Ref. 3, the topological collapse is due to the instantaneous multiple reconnections at different sites on the vortex strands, while the inverse cascade is due to the casual tying of the vortex strands. The latter was observed in Ref. 3, where a trefoil knot was generated by successive reconnections of two unlinked, perturbed rings. As can be seen from the whole spectra of decaying paths shown in Fig. 3, a general trend can be observed in the transition from red to shades of gray, with few minor reversals. A predictive theory for these specific transitions is almost impossible due to the complexity of the nonlinearities involved. However, the overall trend remains clear: the system evolves from a topologically complex state toward a collection of unknots, with inverse transitions being relatively rare and not altering the dominant trajectory. Such a behavior is also observed in

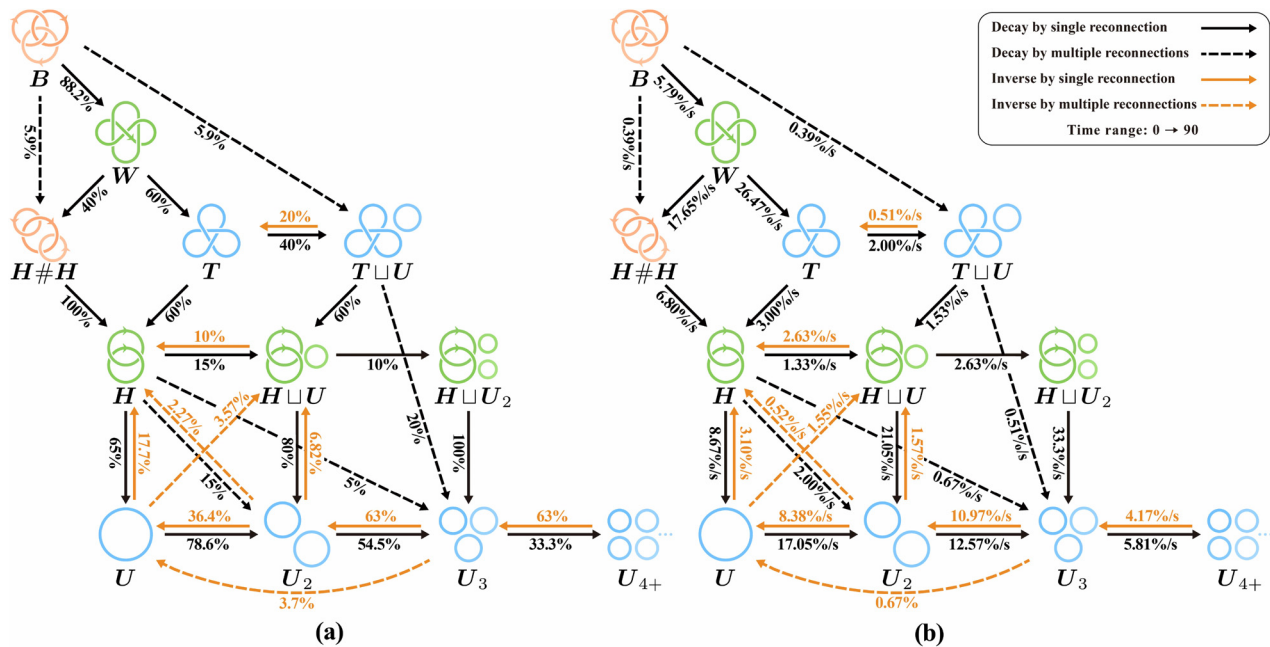


FIG. 6. (a) Probabilities  $P$  and (b) transition rates  $R$  associated with topological transitions. The black arrows denote the *direct topological cascades*, where the solid and dashed lines refer to the single and multiple untying processes, respectively. The orange arrows denote the *inverse topological cascades*, where the solid and dashed lines refer to the single and multiple tying processes, respectively.

simulations of quantum turbulence and confirmed by the knot spectrum analysis carried out in Ref. 21. Insights regarding the irreversibility associated with these transitions can be found in Refs. 11 and 37.

A visual representation of the key routes of topological simplification is shown in Fig. 4. Black arrows denote the possible pathways by a single reconnection, while the colored lines identify the routes associated with the prescribed initial conditions given in the insets. Note that the wiggled lines denoting topologically cyclic jumping<sup>3</sup> take place prevalently in the lower-right part of the diagrams. The direction of knot evolution is primarily governed by two mechanisms: topological simplification and generation of unknots.

From a topological dynamical viewpoint, in agreement with the classification proposed in Ref. 3, the evolution process is roughly composed of several regions, as shown in Fig. 5:

- Type-I of almost-monotonical degeneration (top-left, yellow): Most configurations in this region are of relatively complex topology, and the transitions are dominated by a marked prevalence of direct decays from a higher complexity state to a lower complexity state.
- Type-II of wiggling cyclic evolutions (lower-right, blue): This region is characterized by cyclic productions of a collection of unknotted loops, with a minor possibility of forming Hopf links or even trefoil knots.
- *Region of gradual changing* (in between I and II): As the topology becomes progressively simpler, the generation of unknots begins to challenge the dominance of topological simplification. In this region, the evolution routes exhibit certain reversibility, although reverse-processes remain significantly less frequent than forward-ones. When the system’s primary topology gradually turns to the

trivial unknots, reverse processes, still a minority though, become more and more non-negligible.

The border between the two dynamical regimes, monotonical and wiggling, is also evident from the diagram of Fig. 3, where the transition between the type-I and II regions is marked by the first border from the Hopf Link  $H$  (blue) to the Unknots  $U_n$  (gray).

#### IV. STATISTICS AND BIFURCATION GRAPHS FROM TOPOLOGICAL TRANSITIONS

In order to provide estimates to quantify the prevalence or probability of the observed phenomena, we introduce a simple statistical measure based on the collected data. In this regard, it is convenient to restrict the analysis to the time range  $t \in [0, 90]$ , as shown in Fig. 9 of Appendix B, where most of the interesting transitions occur. Data are, thus, analyzed as per the 91 time units for the 17 angles prescribed represented by the 1547 boxes (snapshots). For this time range, we count a total of 186 topological changes, on the top of which, we examine two quantitative indices:

- *Pathway selection probability*,  $P_{ij} = P(\mathcal{K}_i \rightarrow \mathcal{K}_j) = N_p(\mathcal{K}_i \rightarrow \mathcal{K}_j) / \sum_j N_p(\mathcal{K}_i \rightarrow \mathcal{K}_j)$ . The ratio  $P$  serves as the pathway selection probability associated with each observed topological transition. Here,  $N_p(\mathcal{K}_i \rightarrow \mathcal{K}_j)$  is the number of topological changes happening on a studied *pathway*  $\mathcal{K}_i \rightarrow \mathcal{K}_j$ , from one topological state  $\mathcal{K}_i$  to  $\mathcal{K}_j$ , including those within the topological cycles. Data of  $P$  are presented in Fig. 6(a).
- *Topological transition rate*,  $R_{ij} = R(\mathcal{K}_i \rightarrow \mathcal{K}_j) = N_p(\mathcal{K}_i \rightarrow \mathcal{K}_j) / N(\mathcal{K}_i)R$  is introduced to evaluate the transition frequency along each pathway. Here,  $N(\mathcal{K}_i)$  represents the number of *snapshots*

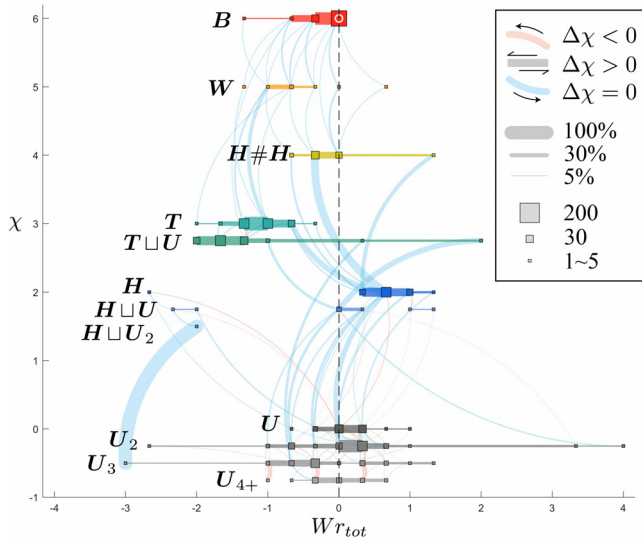


**FIG. 7.** Bifurcation graph illustrating the topological dynamics of evolutionary complexity ( $\chi$ ) as a function of morphology ( $Wr_{tot}$ ), with data spanning values of  $\theta$  from 0 to  $16\pi/48$  and time  $t \in [0, 90]$ . The initial conditions are represented by a white circle located at the top-middle of the graph. The size of each square indicates the number of snapshot data points near a given writhe value for a specific topology, with the area corresponding to the total number of time units (persistence) achieved during the evolution. Horizontal lines represent writhe changes that occur without altering the topology. Light blue lines denote a reduction in evolutionary complexity ( $\Delta\chi < 0$ ), and light orange lines an increase in complexity ( $\Delta\chi > 0$ ). Line thickness reflects the relative proportion of events evolving from one state to another, and thicker lines representing a larger percentage (up to 100%).

associated with a studied topology  $\mathcal{K}_i$  for all specific  $\theta$  (given by the number of time units along the time axis of Fig. 3). Data of  $R$  are shown in Fig. 6(b).  $R$  provides an estimate for the topological persistence of a given state, which further leads to another measure, the average life  $\tau$ , for a given configuration  $\mathcal{K}$  as  $\tau_i = [\sum_j R_{ij}]^{-1}$ . A computational example is  $T \sqcup U$ : its transitions to the trefoil  $T$ , to  $H \sqcup U$ , and to  $U_3$  are relatively slow, accounting for the most persistent events; hence, the average life of  $T \sqcup U$  is computed as  $\tau(T \sqcup U) = (0.51\%/s + .53\%/s + 0.51\%/s)^{-1} = 39.20$  s.

**A. Modified crossing number and dynamical bifurcation graphs**

Two geometric and topological measures of structural complexity provide useful information for understanding subtle features of the dynamical evolution of a vortex tangle. One is the writhe number of a closed space curve  $\mathcal{C}$ , defined by<sup>38</sup>

$$Wr(\mathcal{C}) = \frac{1}{4\pi} \oint_{\mathcal{C}} \oint_{\mathcal{C}} \frac{\mathbf{X} - \mathbf{Y}}{\|\mathbf{X} - \mathbf{Y}\|^3} \cdot (d\mathbf{X} \times d\mathbf{Y}), \tag{7}$$

where  $\mathbf{X}$  and  $\mathbf{Y}$  denote two distinct points on  $\mathcal{C}$ . This is a global geometric measure of the folding and twisting of a loop in space and is a continuous function of the geometry, taking real values. The other is

the Gauss linking number of two closed space curves  $\mathcal{C}_1$  and  $\mathcal{C}_2$ , given by<sup>39</sup>

$$Lk(\mathcal{C}_1, \mathcal{C}_2) = \frac{1}{4\pi} \oint_{\mathcal{C}_1} \oint_{\mathcal{C}_2} \frac{\mathbf{X}_1 - \mathbf{X}_2}{\|\mathbf{X}_1 - \mathbf{X}_2\|^3} \cdot (d\mathbf{X}_1 \times d\mathbf{X}_2), \tag{8}$$

where  $\mathbf{X}_1 \in \mathcal{C}_1$  and  $\mathbf{X}_2 \in \mathcal{C}_2$ . The linking number gives information on the linkage of  $\mathcal{C}_1$  and  $\mathcal{C}_2$  and is a topological invariant of the link, taking only integer values. The centerlines  $C_i$  are extracted from the  $\psi$ -field first by looking for points of minimum density and then by fitting them so as to ensure a smooth line in the three-dimensional space.<sup>2,3,35</sup> A linear combination of  $Wr$  and  $Lk$ , extended to a number  $i = 1, 2, \dots$  of vortices present, provides a useful measure of structural complexity of the tangle; this is the total writhe<sup>40</sup>

$$Wr_{tot} = \sum_i Wr_i(C_i) + \sum_{i \neq j} Lk_{i,j}(C_i, C_j). \tag{9}$$

This quantity is computed for each time step to provide a dynamical information of the tangle evolution.

To capture the topologically evolutionary direction of the system and provide a finer description for the transitions between topological states, we introduce a *modified crossing number*,  $\chi$ , to measure the system’s structural complexity,

$$\chi = n + \chi_s, \tag{10}$$

where  $n$  is the usual minimal crossing number, playing the primary, dominant role in quantifying the topological complexity, whereas  $\chi_s$  is a secondary term standing for a modification,

$$\chi_s = -\epsilon(m - 1), \quad \chi_s < 1, \tag{11}$$

where  $m$  counts the number of knots, links, or unknots in the system at a certain moment. The part  $(m - 1)$ , indeed, refers to the components surrounding the primary knot/link. For instance, in an  $H \sqcup U_2$  state, the total number of components is  $m = 3$ , while those surrounding the primary link  $H$  are the other  $m - 1 = 2$  circles.  $\epsilon$  is an order-controlling parameter, to ensure that  $\chi_s$  remains subordinate to the primary term  $n$  in order, namely,  $\epsilon = o(1)$ . In this work, we adopt  $\epsilon = 0.2$ .

The essence of  $\chi$  is threefold.

- The ambient influence of dominant structures is considered, emphasizing the significant contributions of each non-trivial knot or link to the vortex ensemble.
- When  $m \neq 1$ ,  $\chi_s$  gives rise to a splitting of the dominant crossing number  $n$ , so as to reveal a richer structure containing several refined sub-levels beyond the primary level  $n$  (see the vertical axis of Fig. 7). Typical examples include:  $T$ , which is split into  $T$  and  $T \sqcup U$ ;  $H$ , which is split into  $H$ ,  $H \sqcup U$ , and  $H \sqcup U_2$ ; and  $U$ , which is split into  $U_1$ ,  $U_2$ ,  $U_3$ , and  $U_{4+}$ , sequentially.
- Within the framework of  $\chi$ , one can see more topological transitions taking place in between the new refined sub-states.

Figure 7 reports the time evolution of  $\chi$  against the total writhe  $Wr_{tot}$  for the 17 evolutions in the time range  $t \in [0, 90]$ . Since  $Wr_{tot}$  is a continuous function of the geometry, to facilitate a more direct interpretation of the relationship between  $\chi$  and  $Wr_{tot}$ , we divide the range of  $Wr_{tot}$  into segments of width  $\Delta Wr = \frac{1}{3}$ . For each segment, the number of snapshots is counted and represented by the area of a square

placed at the midpoint of the segment. Since at time  $t = 0$ , the set of Borromean rings is given by three planar ellipses, i.e., the writhe of every single component is zero, the total writhe value is zero, and, thus, the Gauss linking number of the system is also zero, which is a very special case of non-trivial linking.

The graph plotted in Fig. 7 represents a bifurcation diagram of topological dynamics where a number of key features emerge distinctly. First, it illustrates the dominant effects of a direct topological cascade of a complex tangle, providing quantitative information of the relative topological persistence of single events. Second, the marked emergence of trefoil knots, followed by a sea of unknotted loops. Third, the increasing dispersion of writhe values (more extreme convoluted structures form at the expense of topology) as time passes, with the final production (bottom part of the graph) of more and more loops attaining an averaged zero writhe, in agreement with the observed final production of small vortex rings.<sup>2,3</sup>

## V. CONCLUSION

In this paper, we address the question of how a topologically complex system of quantum vortices forming a set of Borromean rings evolves under the Gross–Pitaevskii equation. Numerical simulations have been carried out by employing the Strang time splitting Fourier method. Among the possible ways of generating a set of initial conditions that differ by a geometric parameter, we have chosen to vary the tilting angle of one ring, thus obtaining 17 different evolutionary pathways. Each path has been analyzed in great detail in terms of topology and structural complexity, observing 186 instances of topological changes due to the reconnection events occurred during the time evolution.

With this work, we have discovered and proven several interesting results. Starting from a relatively complex tangle of vortices, we confirm that the decay process is dominated by a direct topological cascade driven by a continuous topological simplification of the tangle toward the production of unlinked, unknotted loops. This result is in good agreement with earlier studies<sup>3,2,3</sup> of decaying quantum vortex defects, a feature shared by classical turbulence as well. In agreement with the observations of Ref. 21, inverse topological cascades do occur as well, but they represent rare events that tend to happen in secondary regimes of mixed topological cycles, when interactions between simple unknotted loops are dominant (see Figs. 4 and 5). The chart of Fig. 3 and the diagrams of Fig. 6 provide quantitative measurements of the observations. Figure 7, by reporting a modified crossing number  $\chi$  that contains the usual  $n$ -part delivering the tangling and linking information of a vortex system, and an extra  $\chi_s$ -part that incorporates unlinked vortex clusters in relation to cascade fragmentation, confirms that trefoil knots tend to be relatively persistent, and writhe values tend to get dispersed over time, with the mean value distributing around zero in the last evolutionary stages of the process. Since zero writhe is a signature of planarity, this confirms the overall trend toward the generation of small-scale planar loops (rings). Such a comprehensive representation not only distinguishes a broader spectrum of topological states beyond the typical archetypes but also provides a more convenient and precise tool to capture the evolutionary scenario, thus making the modified crossing number  $\chi$  possibly suitable for applications beyond the current study.

The trend that leads structures to undergo free evolution through topological simplification therefore becomes an established fact and the main result of this paper. The implication of this generic behavior in energy transfers is a question under investigation, which we hope to be able to address in a subsequent paper.

## ACKNOWLEDGMENTS

The authors are indebted to Professor Renzo L. Ricca for helpful discussion and useful advice. X.L. wishes to acknowledge financial support from the Beijing Natural Science Foundation (Grant Nos. IS23030 and Z180007) and the National Natural Science Foundation of China (Grant No. 11572005). H.G. wishes to acknowledge financial support from the China Scholarship Council (No. 202106540044).

## AUTHOR DECLARATIONS

### Conflict of Interest

The authors have no conflicts to disclose.

### Author Contributions

**Hao Guan:** Conceptualization (equal); Data curation (lead); Formal analysis (lead); Investigation (lead); Methodology (lead); Software (equal); Visualization (lead); Writing – original draft (lead); Writing – review & editing (equal). **Simone Zuccher:** Software (equal); Visualization (supporting); Writing – review & editing (equal). **Xin Liu:** Conceptualization (equal); Funding acquisition (lead); Supervision (lead); Visualization (supporting); Writing – original draft (supporting); Writing – review & editing (equal).

## DATA AVAILABILITY

The data that support the findings of this study are available within the article.

## APPENDIX A: TOPOLOGICAL TRANSITION CHART

Figure 8 shows all the admissible topological transitions that the Borromean rings may undergo from the mathematical point of view, based on the analysis of the minimal diagram projections of knot theory.<sup>39</sup> According to the relative strand orientations, we can distinguish different knot types identified by the positive and negative Whitehead links  $W_{\pm}$ , the figure-of-eight knot  $F^8$ , the right- and left-handed trefoil knot  $T^{R/L}$ , the positive and negative Hopf link  $H_{\pm}$ , and their various disjoint union of these topological types. The dashed arrows denote the transitions admissible in theory but not observed in the 17 experiments, whereas the thickened band arrows denote the actual topological transitions observed in the simulations.

The focus of this paper is on the cascade process of quantum vortex knots system. The underlying knot theory and statistical mechanics origins will be discussed in detail in a separate paper.

## APPENDIX B: TOPOLOGICAL CASCADE IN THE TIME RANGE $t \in [0, 90]$

Restricting the topological analysis to the time range  $t \in [0, 90]$  (see Fig. 9), we can identify four different regions, separated by the



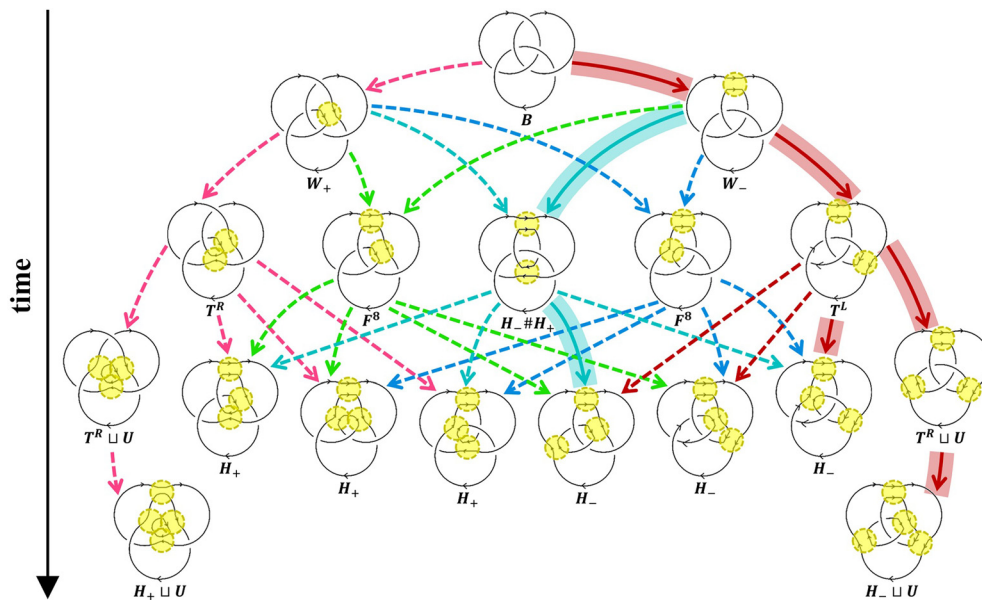


FIG. 8. Pictorial representation of the admissible topological transitions possible in theory. Thickened band arrows denote the actual topological cascades observed in the simulation.

dashed lines  $\alpha$ ,  $\beta$ , and  $\gamma$ . These regions capture the topological persistence of the key topological configurations observed throughout the simulations. The narrow region between the  $\alpha$ - and  $\beta$ -curve highlights the brief transient production of 5- and 4-crossing structures and

marks the rapid passage to the formation of trefoil knots and Hopf links. The green area is made of trefoil knots and single unknots with equal “probability” distribution (marked by the  $\gamma$ -curve), till the final production of several unknots that populate the shades of gray area.

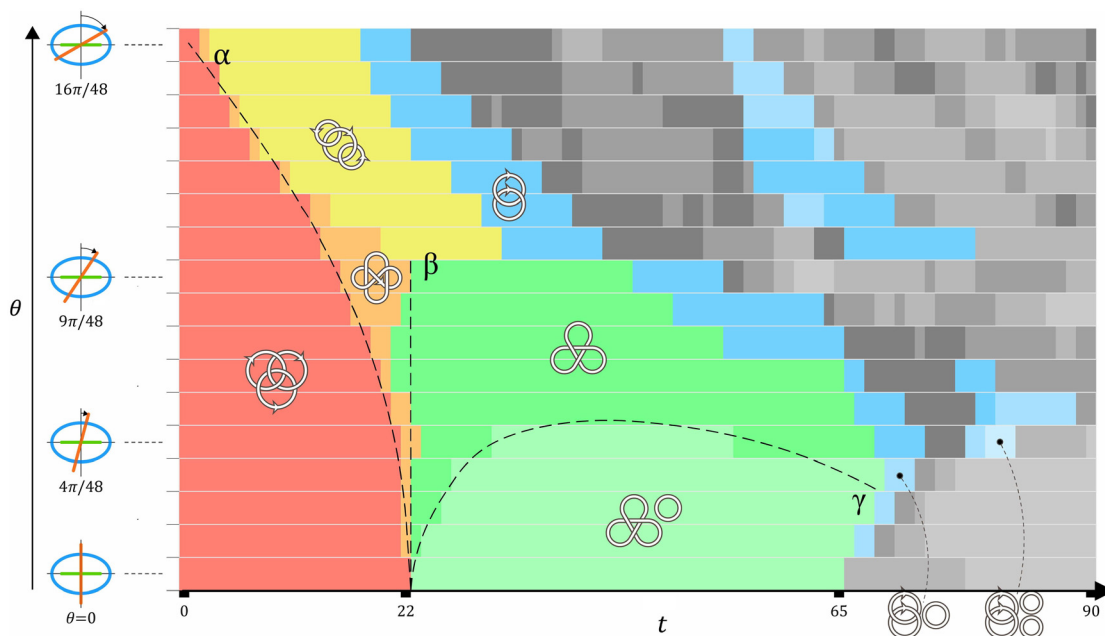


FIG. 9. Topological cascade of the Borromean rings by various values of  $\theta$ , from 0 to  $16\pi/48$ , restricted to the time range  $t \in [0, 90]$ .

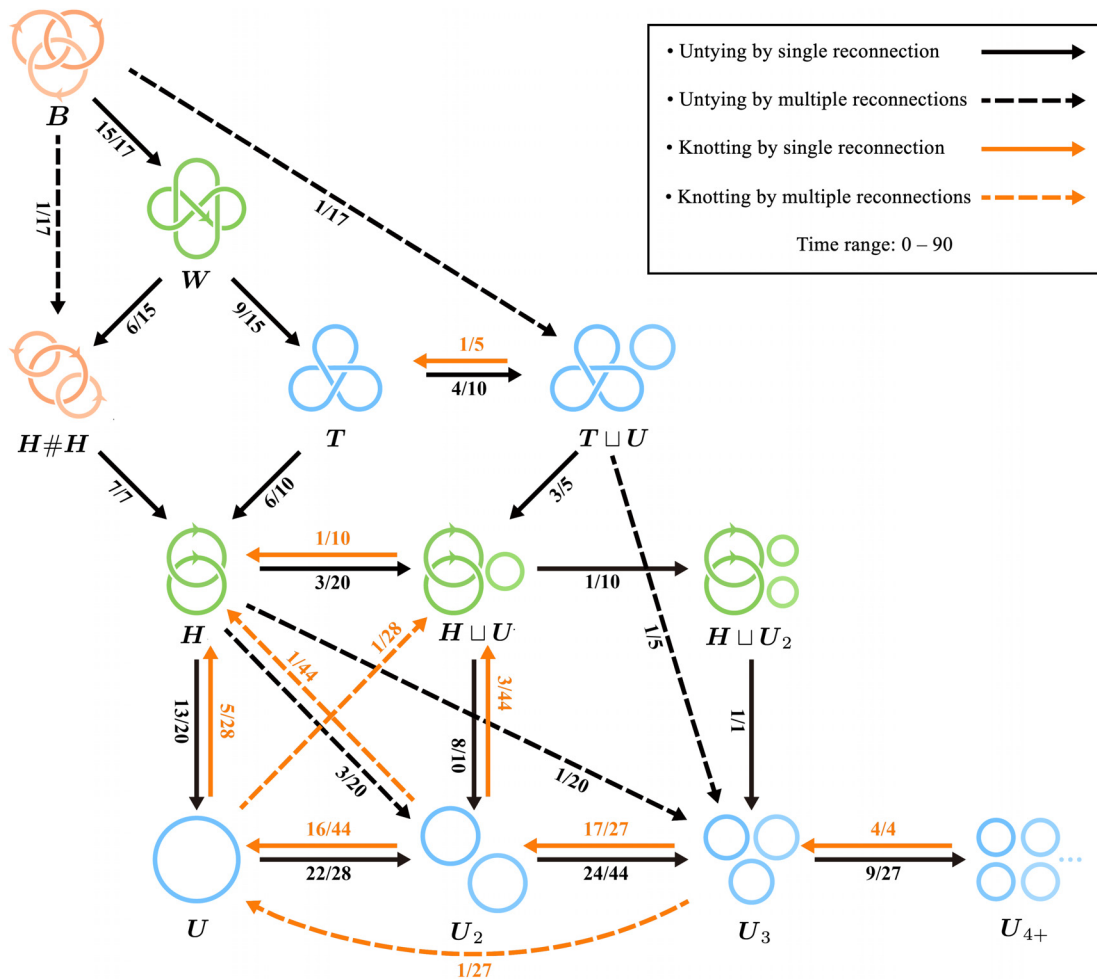


FIG. 10. Computation of the probability  $P_i$  of topological transitions based on the numbers  $N_c$  and  $N_r$  of topological changes and reconnections occurring along pathways.

APPENDIX C: PROBABILITY OF TOPOLOGICAL TRANSITION

Computation of the probability  $P_{ij} = P(\mathcal{K}_i \rightarrow \mathcal{K}_j)$  associated with a single topological transition  $\mathcal{K}_i \rightarrow \mathcal{K}_j$  is based on the numbers  $N_p(\mathcal{K}_i \rightarrow \mathcal{K}_j)$  and  $\sum_j N_p(\mathcal{K}_i \rightarrow \mathcal{K}_j)$  of topological changes and reconnections observed. For example, the total number of reconnections observed for the transitions of the Borromean rings  $B$  to produce  $H \# H$ ,  $W$ , and  $T \sqcup U$  is 17, only one of which determines the production of  $H \sqcup H$  and one the production of  $T \sqcup U$ ; the remaining 15 lead to the formation of the Whitehead link  $W$ . We have

$$\begin{aligned}
 P(B \rightarrow H \# H) &= \frac{N_p(B \rightarrow H \# H)}{N_p(B \rightarrow H \# H) + N_p(B \rightarrow W) + N_p(B \rightarrow T \sqcup U)} \\
 &= \frac{1}{1 + 15 + 1} = \frac{1}{17} = 5.9\%, \tag{C1}
 \end{aligned}$$

where  $\sqcup$  stands for disjoint union and  $\#$  the direct sum (Fig. 10).

REFERENCES

- <sup>1</sup>S. Zuccher, M. Caliarì, A. W. Baggaley, and C. F. Barenghi, “Quantum vortex reconnections,” *Phys. Fluids* **24**, 125108 (2012).
- <sup>2</sup>S. Zuccher and R. L. Ricca, “Relaxation of twist helicity in the cascade process of linked quantum vortices,” *Phys. Rev. E* **95**, 053109 (2017)
- <sup>3</sup>S. Zuccher and R. L. Ricca, “Creation of quantum knots and links driven by minimal surfaces,” *J. Fluid Mech.* **942**, A8 (2022).
- <sup>4</sup>R. L. Ricca, “Topological fluid dynamics and knotted fields,” in *Encyclopedia of Mathematical Physics*, 2nd ed., edited by R. Szabo and M. Bojowald (Academic Press, Oxford, 2025), pp. 245–255.
- <sup>5</sup>W.-K. Bai, J.-C. Xing, T. Yang, W.-L. Yang, and W.-M. Liu, “Nonlinear dynamics of a Bose-Einstein condensate excited by a vortex ring phase imprinting,” *Results Phys.* **22**, 103828 (2021).
- <sup>6</sup>S. Zou, W.-K. Bai, T. Yang, and W.-M. Liu, “Formation of vortex rings and hopfions in trapped Bose-Einstein condensates,” *Phys. Fluids* **33**, 027105 (2021).
- <sup>7</sup>M. Tsubota, S. Ogawa, and Y. Hattori, “Vortex reconnection and acoustic emission by the numerical analysis of the Gross-Pitaevskii equation,” *J. Low Temp. Phys.* **121**, 435–440 (2000).
- <sup>8</sup>S. Z. Alamri, A. J. Youd, and C. F. Barenghi, “Reconnection of superfluid vortex bundles,” *Phys. Rev. Lett.* **101**, 215302 (2008).

- <sup>9</sup>C. Rorai, J. Skipper, R. M. Kerr, and K. R. Sreenivasan, "Approach and separation of quantised vortices with balanced cores," *J. Fluid Mech.* **808**, 641–667 (2016).
- <sup>10</sup>L. Galantucci, A. W. Baggaley, N. G. Parker, and C. F. Barenghi, "Crossover from interaction to driven regimes in quantum vortex reconnections," *Proc. Natl. Acad. Sci. U. S. A.* **116**, 12204–12211 (2019).
- <sup>11</sup>A. Villosio, D. Proment, and G. Krstulovich, "Irreversible dynamics of vortex reconnections in quantum fluids," *Phys. Rev. Lett.* **125**, 164501 (2020).
- <sup>12</sup>T. Nakagawa, S. Inui, and M. Tsubota, "Internal structure of localized quantized vortex tangles," *Phys. Rev. B* **104**, 094510 (2021).
- <sup>13</sup>J. Zylberman, G. D. Molfetta, M. Brachet, N. F. Loureiro, and F. Debbasch, "Quantum simulations of hydrodynamics via the Madelung transformation," *Phys. Rev. A* **106**, 032408 (2022).
- <sup>14</sup>Y. Zhu, B. Semisalov, G. Krstulovic, and S. Nazarenko, "Direct and inverse cascades in turbulent Bose-Einstein condensates," *Phys. Rev. Lett.* **130**, 133001 (2023).
- <sup>15</sup>C. F. Barenghi, H. A. J. Middleton-Spencer, L. Galantucci, and N. G. Parker, "Types of quantum turbulence," *AVS Quantum Sci.* **5**, 025601 (2023).
- <sup>16</sup>C. F. Barenghi, L. Skrbek, and K. R. Sreenivasan, *Quantum Turbulence* (Cambridge University Press, Cambridge, 2023).
- <sup>17</sup>M. Klawunn and L. Santos, "Phase transition from straight into twisted vortex lines in dipolar Bose-Einstein condensates," *New J. Phys.* **11**, 055012 (2009).
- <sup>18</sup>A. Villosio, D. Proment, and G. Krstulovic, "Evolution of a superfluid vortex filament tangle driven by the Gross-Pitaevskii equation," *Phys. Rev. E* **93**, 061103 (2016).
- <sup>19</sup>P. C. di Leoni, P. D. Mininni, and M. E. Brachet, "Helicity, topology, and Kelvin waves in reconnecting quantum knots," *Phys. Rev. A* **94**, 043605 (2016).
- <sup>20</sup>M. Foresti and R. L. Ricca, "Instability of a quantum vortex by twist perturbation," *J. Fluid Mech.* **949**, A19 (2022).
- <sup>21</sup>R. G. Cooper, M. Mesgarnezhad, A. W. Baggaley, and C. F. Barenghi, "Knot spectrum of turbulence," *Sci. Rep.* **9**, 10545 (2019).
- <sup>22</sup>C. F. Barenghi, "Tangled vortex lines: Dynamics, geometry and topology of quantum turbulence," in *Knotted Fields*, edited by R. L. Ricca and X. Liu (Springer Nature Switzerland, Cham, 2024), pp. 243–279.
- <sup>23</sup>D. Kleckner, L. H. Kauffman, and W. T. M. Irvine, "How superfluid vortex knots untie," *Nat. Phys.* **12**, 650–655 (2016).
- <sup>24</sup>W.-K. Bai, T. Yang, and W.-M. Liu, "Topological transition from superfluid vortex rings to isolated knots and links," *Phys. Rev. A* **102**, 063318 (2020).
- <sup>25</sup>D. Kleckner and W. T. M. Irvine, "Creation and dynamics of knotted vortices," *Nat. Phys.* **9**, 253–258 (2013).
- <sup>26</sup>J.-H. Hao and Y. Yang, "Magnetic knot cascade via the stepwise reconnection of helical flux tubes," *J. Fluid Mech.* **912**, A48 (2021).
- <sup>27</sup>F. H. W.-Y. Shen, J. Yao, and Y. Yang, "Topological transition and helicity conversion of vortex knots and links," *J. Fluid Mech.* **943**, A41 (2022).
- <sup>28</sup>K. Shimokawa, K. Ishihara, I. Grainge, D. J. Sherratt, and M. Vazquez, "Ftsk-dependent XerCD-*diff* recombination unlinks replication catenanes in a stepwise manner," *Proc. Natl. Acad. Sci. U. S. A.* **110**, 20906–20911 (2013).
- <sup>29</sup>R. Stolz, M. Yoshida, R. Brasher, M. Flanner, K. Ishihara, D. J. Sherratt, K. Shimokawa, and M. Vazquez, "Pathways of DNA unlinking: A story of stepwise simplification," *Sci. Rep.* **7**, 12420 (2017).
- <sup>30</sup>X. Liu, R. L. Ricca, and X.-F. Li, "Minimal unlinking pathways as geodesics in knot polynomial space," *Commun. Phys.* **3**, 136 (2020).
- <sup>31</sup>L. P. Pitaevskii and S. Stringari, *Bose-Einstein Condensation*, 1st ed., International Series of Monographs on Physics Vol. 116 (Clarendon Press, Oxford, 2003).
- <sup>32</sup>C. F. Barenghi and N. G. Parker, *A Primer on Quantum Fluids*, 1st ed., SpringerBriefs in Physics Vol. 1 (Springer Cham, Cham, 2016).
- <sup>33</sup>M. Caliari and S. Zuccher, "INFFTM: Fast evaluation of 3D Fourier series in MATLAB with an application to quantum vortex reconnections," *Comput. Phys. Commun.* **213**, 197–207 (2017).
- <sup>34</sup>M. Caliari and S. Zuccher, "Reliability of the time splitting Fourier method for singular solutions in quantum fluids," *Comput. Phys. Commun.* **222**, 46–58 (2018).
- <sup>35</sup>M. Caliari and S. Zuccher, "A fast time splitting finite difference approach to Gross-Pitaevskii equations," *Commun. Comput. Phys.* **29**, 1336–1364 (2021).
- <sup>36</sup>X. Liu, R. L. Ricca, and H. Guan, "A topological approach to vortex knots and links," in *Knotted Fields*, edited by R. L. Ricca and X. Liu (Springer Nature Switzerland, Cham, 2024).
- <sup>37</sup>P. Z. Stasiak, Y.-M. Xing, Y. Alihosseini, C. F. Barenghi, A. Baggaley, W. Guo, L. Galantucci, and G. Krstulovic, "Experimental and theoretical evidence of universality in superfluid vortex reconnections," [arXiv:2411.08942](https://arxiv.org/abs/2411.08942) (2024).
- <sup>38</sup>F. B. Fuller, "The writhing number of a space curve," *Proc. Natl. Acad. Sci. U. S. A.* **68**, 815–819 (1971).
- <sup>39</sup>C. C. Adams, *The Knot Book: An Elementary Introduction to the Mathematical Theory of Knots*, 1st ed. (W. H. Freeman & Co., New York, 1994).
- <sup>40</sup>C. E. Laing, R. L. Ricca, and D. W. L. Summers, "Conservation of writhe helicity under anti-parallel reconnection," *Sci. Rep.* **5**, 9224 (2015).